

Surface Spectral Emissivity Derived from MODIS Data

Yan Chen, Sunny Sun-Mack
SAIC, Hampton, VA USA

Patrick Minnis, David F. Young, William L. Smith, Jr.
Atmospheric Sciences, NASA Langley Research Center, Hampton, VA USA

Extended Abstract for
*SPIE 3rd International Asia-Pacific Environmental Remote Sensing Symposium 2002:
Remote Sensing of the Atmosphere, Ocean, Environment, and Space*
Hangzhou, China
October 23-27, 2002

Surface spectral emissivity derived from MODIS data

Yan Chen^a, Sunny Sun-Mack^a, Patrick Minnis^{*b}, William L. Smith, Jr.^b, David F. Young^b

^aScience Applications International Corporation, Hampton, VA 23666

^bAtmospheric Sciences, NASA Langley Research Center, Hampton, VA 23681

ABSTRACT

Surface emissivity is essential for many remote sensing applications including the retrieval of the surface skin temperature from satellite-based infrared measurements, determining thresholds for cloud detection and for estimating the emission of longwave radiation from the surface, an important component of the energy budget of the surface-atmosphere interface. In this paper, data from the Terra MODIS (MODerate-resolution Imaging Spectroradiometer) taken at 3.7, 8.5, 10.8, 12.0 μm are used to simultaneously derive the skin temperature and the surface emissivities at the same wavelengths. The methodology uses separate measurements of the clear-sky temperatures that are determined by the CERES (Clouds and Earth's Radiant Energy System) scene classification in each channel during the daytime and at night. The relationships between the various channels at night are used during the day when solar reflectance affects the 3.7- μm data. A set of simultaneous equations is then solved to derive the emissivities. Global results are derived from MODIS. Numerical weather analyses are used to provide soundings for correcting the observed radiances for atmospheric absorption. These results are verified and will be available for remote sensing applications.

Keywords: MODIS, CERES, VIRS, ISCCP DX, emissivity, surface, radiation, brightness temperature

1. INTRODUCTION

Surface emissivity is essential for many remote sensing applications. It is also critical for deriving the surface skin temperature from satellite-based infrared measurements, determining thresholds for cloud detection and for estimating the emission of longwave radiation from the surface, an important component of the energy budget of the surface-atmosphere interface. It is also critical for cloud detection and retrieval of cloud properties. Brightness temperature differences BTD between 3.7 and 10.8- μm observations are often indicative of the presence or absence of clouds. For clear scenes, the BTD is due to differences in atmospheric absorption and in surface emissivity ϵ between the two channels. Cloud phase, optical depth, and particle size further affect the BTD in cloudy scenes. Retrieval of cloud phase and effective particle size often relies on the value of BTD, which for optically thin clouds is affected by the surface emission and, at 3.7 μm , the surface reflectance. Thus, the accuracy of cloud detection and particle size retrievals depends on the accuracy of the surface emissivity. The Clouds and Earth's Radiant Energy System (CERES) system [1] is measuring broadband shortwave and longwave radiances and deriving cloud properties from various imagers to produce a combined global radiation and cloud property data set [2]. This paper presents the development and results of an analysis of satellite imager data taken at 3.7, 8.5, 10.8, and 12.0 μm to derive a monthly map of ϵ for use by CERES and other cloud retrieval algorithms.

2. DATA

Nighttime and daytime MODIS data taken during April of 2001 were analyzed with the CERES cloud processing algorithms [2]. Each MODIS pixel is classified as either clear or cloudy using the latest update of the CERES method [3] to obtain the clear-sky top-of-the-atmosphere (TOA) brightness temperatures T_i at 3.7, 10.8, 12.0, and 8.5 μm , denoted channels $i = 3, 4, 5,$ and $6,$ respectively. MODIS data have a nominal resolution of 1 km but are sampled every

*Corresponding author address: P.Minnis, MS 420 NASA Langley Research Center, Hampton, VA 23681
Email address: p.minnis@larc.nasa.gov

2 km for CERES. It is assumed that the scene classification by the method mentioned above is correct for all pixels and, therefore, the temperatures are uncontaminated by clouds. However, that is not always the case at night and some filtering is required. ECMWF (European Center Medium Range Weather Forecast) analyses provided every 6 hours at a resolution of 1° latitude and longitude were used to specify vertical profiles of atmospheric temperature, humidity, and ozone as well as initial values of surface skin temperature. Linear interpolation was used to match the soundings to the satellite observation times. Standard atmospheric values were used for profiles of other absorbing gases such as NO₂ and CH₄.

3. METHODOLOGY

The basic approach solves a set of simultaneous equations to obtain surface emissivity and follows from earlier work [4, 5]. The method requires observations from both daytime and nighttime over the same area. The relationship between the TOA and surface radiances can be crudely represented as

$$B_i(T_i) = \epsilon_{ai}B_i(T_{ai}) + (1 - \epsilon_{ai})B_i(T_{si}) \quad (1)$$

where B is the Planck function, ϵ_a and T_a are the atmospheric effective emissivity and effective temperature, respectively. The radiance for T_{si} , the effective skin radiating temperature, is determined using the correlated k -distribution method [6] with the atmospheric profiles to remove the molecular absorption. The k -distribution technique is used to compute the downwelling and upwelling radiation at each ECMWF layer over the entire band pass of the channel using the appropriate filter function for the particular satellite imager channel. Considering the downwelling atmospheric radiance at the surface L_{ai} , the radiation balance at surface is

$$B_i(T_{si}) = \epsilon_i B_i(T_{skin}) + (1 - \epsilon_i)L_{ai} \quad (2)$$

in the absence of solar radiation, where T_{skin} is the surface skin temperature. For simplicity, it is assumed that ϵ_i does not depend on the viewing zenith angle VZA. Skin temperature can be expressed at night as

$$T_{skin} = B_i^{-1}[\{B_i(T_{si}) - L_{ai}\} / \epsilon_i + L_{ai}], \quad (3)$$

where B_i^{-1} is the inverse Planck function. If the skin temperature is known, the emissivity can be solved for the remaining channels, e.g.,

$$\epsilon_3 = [B_3(T_{s3}) - L_{a3}] / [B_3(T_{skin}) - L_{a3}]. \quad (4)$$

At night, both T_{s3} and T_{s4} can be derived using (2) and the emissivity ratio,

$$\epsilon_3' = \epsilon_3 / \epsilon_4 = [B_3(T_{s3}) - L_{a3}] / [B_3(T_{s4}) - L_{a3}], \quad (5)$$

can be computed. If it is assumed that this ratio is a constant for a given location during both day and night, then the value of ϵ_3 can be determined from data taken during the daytime. However, the ratio is variable depending on L_{a3} , which changes with the column precipitable water PW. To account for this variation, the data are fitted to

$$\epsilon_3' = \epsilon_{3o}' + a PW + b PW^2, \quad (6)$$

where ϵ_{3o}' is the baseline emissivity ratio and is generally close to the value obtained from (5) if $L_{a3} = 0$. The coefficients for (6) are computed from data taken during the night for all available clear cases during a month to obtain a reasonable dynamic range in PW. During the daytime, the apparent surface temperature for channel 3 is

$$B_3(T_{s3}) = \epsilon_3 [B_3(T_{skin})] + \alpha_3 [\chi S_3' + L_{a3}], \quad (7)$$

where χ is the anisotropic correction factor, α_3 is the surface albedo, and S_3' , the solar radiation reaching the surface, is computed from the Earth-sun distance and solar-zenith-angle corrected solar constant attenuated by atmospheric absorption using the k -distribution method. If the albedo does not vary with incidence angle, then according to the Kirchoff's law,

$$\alpha_3 = (1 - \epsilon_3). \quad (8)$$

Using (4), (5), and (8) to substitute for the emitted component and the albedo on the right hand side of (7) and rearranging gives

$$\epsilon_3 = 1 - \{B_3(T_{s3}) - \epsilon_3' [B_3(T_{s4})] - (1 - \epsilon_3') L_{a3}\} / \chi S_3'. \quad (9)$$

In this manner, ϵ_3 is derived using (9). The absorption coefficients used for the thermal component are applied to the observed 3.7- μm radiance to obtain $B_3(T_{s3})$. Although the atmospheric attenuation of the upwelling solar and emitted 3.7- μm radiances is slightly different for each component, the differences should have a negligible impact on the result. Knowing ϵ_3 , T_{skin} can easily be solved from (7). Then, ϵ_4 , ϵ_5 , and ϵ_6 are computed from (3).

This technique was tested theoretically using 3 different surface types with ϵ_3 ranging from 0.73 to 0.97 and ϵ_4 ranging 0.93 to 0.99 using 91 soundings to represent a large range of atmospheric conditions. Previously, ISCCP (International Satellite Cloud Climatology Project DX Advanced Very High Resolution Radiometer (AVHRR) data [7] taken during 1986 were processed using the same method as mentioned above to obtain channel 3, 4, and 5 emissivity maps. The resulting values of ϵ_3 from ISCCP DX data were within 1% of the original value for all of the cases with the largest errors occurring for the desert (0.73) case. RMS errors up to 3% were found for ϵ_4 with the greatest errors occurring for the desert case. The mean errors were all negligible. The theoretical calculations assumed an isotropic surface reflectance and no VZA-dependence of ϵ .

The MODIS data were analyzed by computing ϵ_3' for each clear nighttime pixel and averaging the results for every 1° latitude-longitude box for a given orbit. The corresponding value of PW was saved for each average. Because of insufficient sampling, however, a mean value of ϵ_3' was computed for each region and used instead of a fit to (6) to derive ϵ_i for all channels from the daytime data to obtain means and standard deviations for each region. The values of χ used in (9) were taken from the models used in the cloud mask [3]. Those models are generally used for visible or

Table 1. IGBP surface type.

1. evergreen needleleaf = conifer	2. evergreen broadleaf = conifer
3. deciduous needleleaf = deciduous	4. deciduous broadleaf = deciduous
5. mixed forests = 1/2 conifer + 1/2 deciduous	6. closed shrublands = mosaic
7. open shrubland = mosaic	8. woody savannas = grass
9. savannas = grass	10. grasslands = grass
11. permanent wetlands = 1/2 grass + 1/2 water	12. croplands = grass
13. urban = black body	14. mosaic = 1/2 grass + 1/2 mixed forest
15. snow/ice	16. barren/sparsely vegetated = desert
17. water	18. tundra = frost
19. coastline = 10% to 90% water	

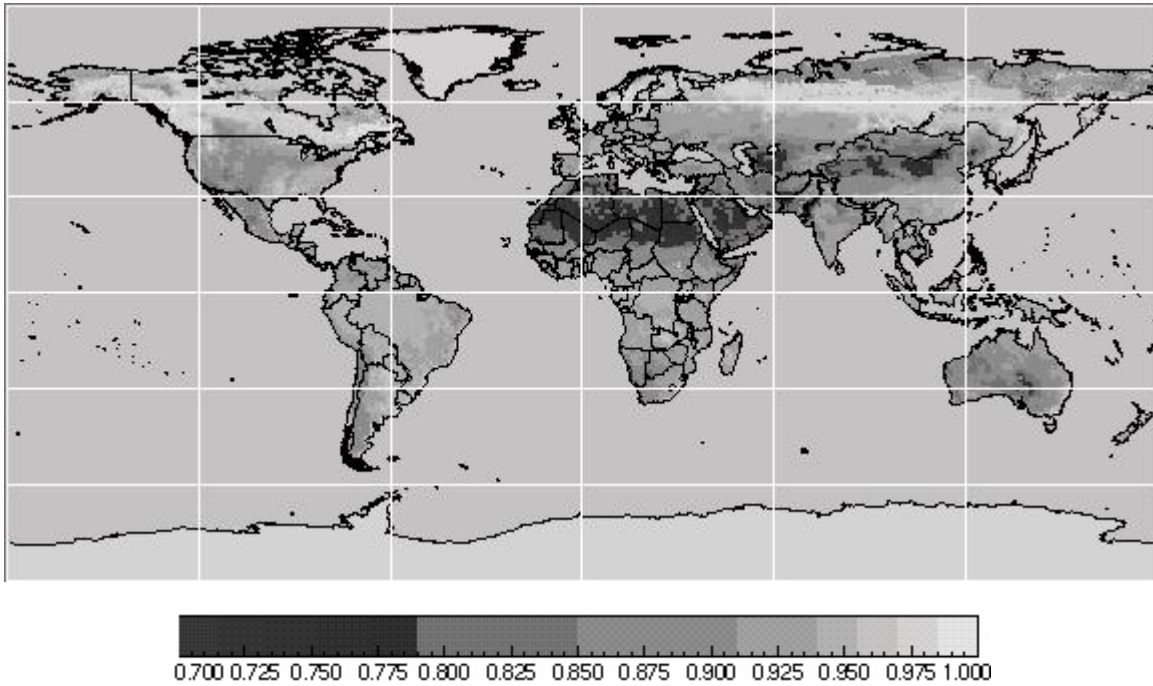


Fig. 1. Mean 3.7- μm surface emissivity derived from MODIS data during April 2001

broad-band solar channels. Averages were also computed for each IGBP surface type (Table 1) and then used to fill in the results for regions with no data. These averages were only computed after filtering the regional results for unrealistic points that can arise due to poor representation of the actual temperature and humidity profiles by the ECMWF reanalyses, the presence of aerosols, or to cloud contamination. The filters were applied by creating histograms of ϵ for each wavelength and IGBP type. Upper (1.0) and lower thresholds were set for each IGBP type and wavelength. MODIS data from April 2001 were processed in this manner. Results are compared to similar analyses applied to data from the Tropical Rainfall Measuring Mission Visible Infrared Scanner (VIRS) and the 1986 AVHRR DX data [4].

4. RESULTS

Figure 1 shows the distribution of ϵ_3 derived with the CERES algorithm from MODIS data taken during April 2001. The gray scale starts at 0.700 although several desert areas have lower values. The heavily vegetated areas have values greater than 0.925 while intermediate values are found over less vegetated regions.

Figures 2, 3, 4 show the distributions of ϵ_4 , ϵ_5 , and ϵ_6 derived from the same data set. The gray scale starts at 0.800 for ϵ_4 , 0.900 for ϵ_5 , and 0.700 for ϵ_6 . The values for ϵ_4 and ϵ_5 were generally much greater than their ϵ_3 counterparts, while the values for ϵ_6 are between ϵ_3 and ϵ_4 . The mean emissivities for each channel are summarized in Table 2 for each of the IGBP types in the Northern Hemisphere. The ocean and snow categories are probably cloud contaminated and are not used for CERES. Instead, a theoretical model [8] is used for water surfaces. A theoretical snow model described was developed for application to snow and sea ice. This theoretical emissivity model is based on adding-doubling radiative transfer calculations that assume the snow can be represented as an ice cloud with an optical depth of 100 composed of a hexagonal ice column with an aspect ratio of $750 \mu\text{m} / 300 \mu\text{m}$.

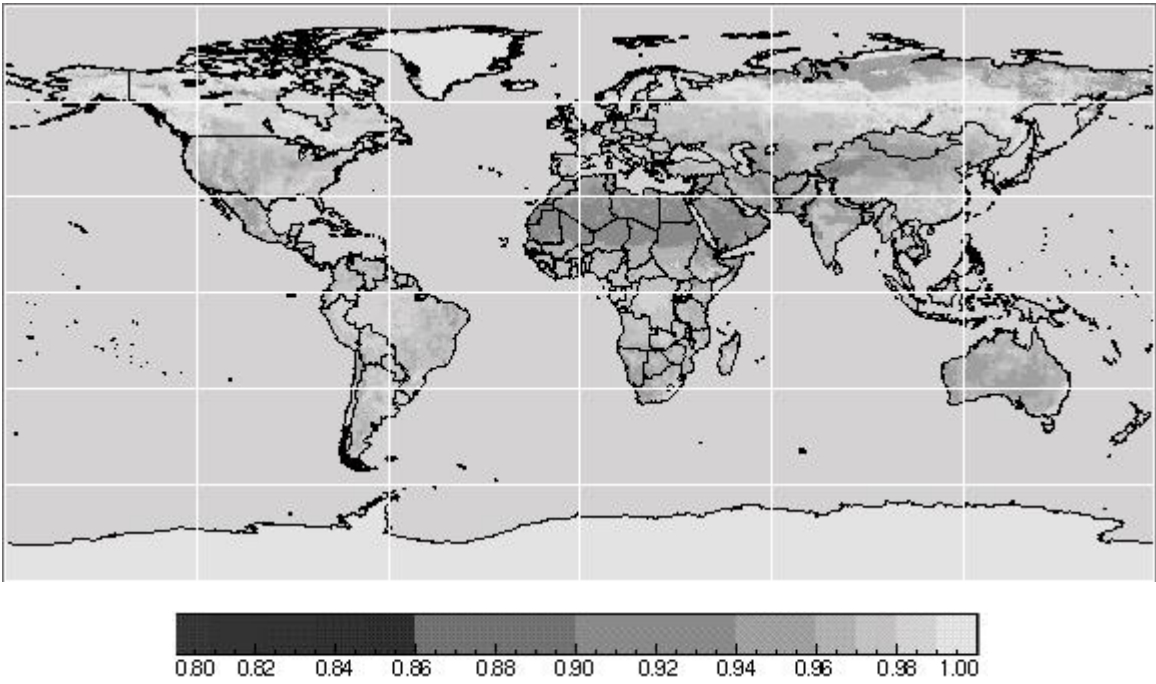


Fig. 2. Monthly mean 10.8- μm surface emissivity derived from MODIS data during 2001

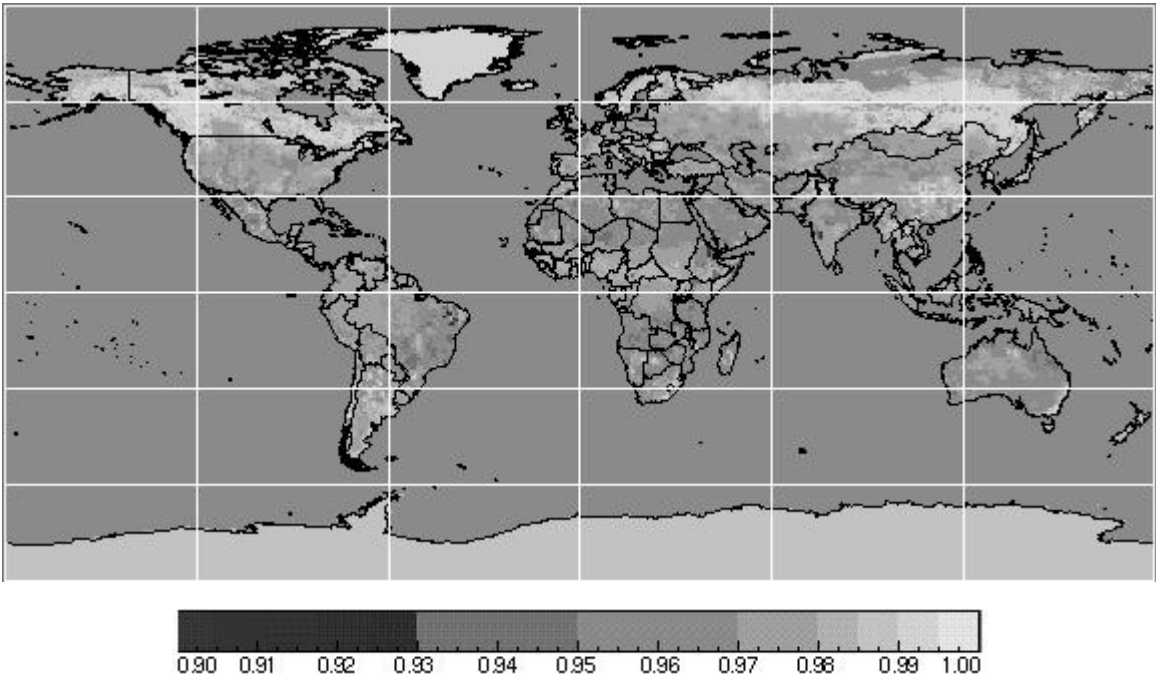


Fig. 3. Monthly mean 12.0- μm surface emissivity derived from MODIS data during 2001

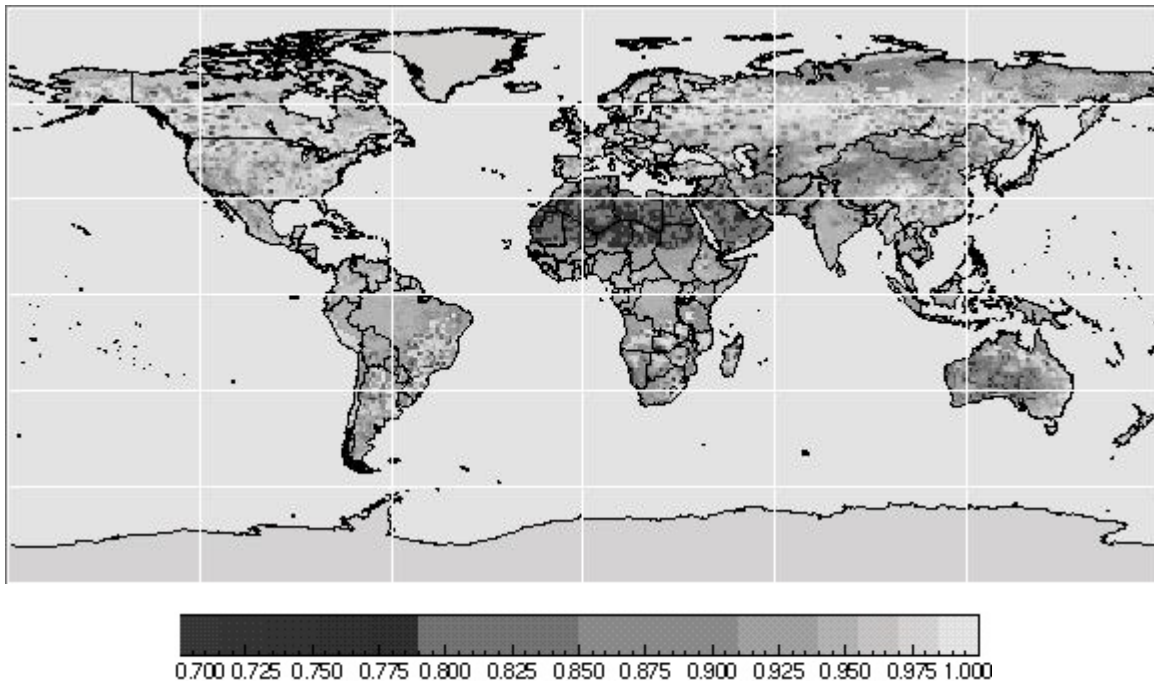


Fig. 4. Monthly mean 8.5- μ m surface emissivity derived from MODIS data during 2001

Table 2. Mean ϵ for Northern Hemisphere.

IGBP Type	3.7 μ m Emissivity	10.8 μ m Emissivity	12.0 μ m Emissivity	8.5 μ m Emissivity
1	0.9647	0.9894	0.9902	0.9589
2	0.9329	0.9742	0.9731	0.9596
3	0.9685	0.9924	0.9960	0.9658
4	0.9440	0.9811	0.9818	0.9596
5	0.9638	0.9887	0.9913	0.9571
6	0.9390	0.9833	0.9849	0.9416
7	0.8503	0.9572	0.9688	0.8899
8	0.9369	0.9801	0.9830	0.9474
9	0.9014	0.9657	0.9701	0.9263
10	0.8910	0.9690	0.9748	0.9338
11	0.9758	0.9955	0.9973	0.9656
12	0.9193	0.9725	0.9758	0.9417
13	0.9264	0.9757	0.9748	0.9436
14	0.9261	0.9760	0.9781	0.9484
15	0.9718	0.9946	0.9909	0.9715
16	0.7692	0.9368	0.9639	0.7806
17	0.9637	0.9775	0.9431	0.9967
18	0.9671	0.9931	0.9881	0.9615
19	0.9533	0.9849	0.9823	0.9571

To assess the results, the clear sky TOA channel-3 brightness temperatures were calculated using the emissivity maps for channels 3 and 4, the observed values of T_4 , and the ECMWF profiles. Three emissivity maps generated from April 2001 MODIS data with CERES algorithm, April 1986 from ISCCP DX data, and April 2001 from Visible Infrared Scanner (VIRS) data with CERES algorithm were applied to April 2001 VIRS data daytime and nighttime separately. The VIRS brightness temperatures were corrected in the following manner to match the expected differences between VIRS and MODIS based on calibration observations and modeling [9].

$$T_3(\text{VIRS new}) = T_3(\text{VIRS old}) - 0.3 \text{ K}, \quad (10)$$

$$T_4(\text{VIRS new}) = T_4(\text{VIRS old}) + 0.5 \text{ K}, \quad (11)$$

and

$$T_5(\text{VIRS new}) = T_5(\text{VIRS old}) + 0.4 \text{ K}. \quad (12)$$

Differences between the predicted and observed values of T_3 are summarized in Table 3. Except for snow, tundra, woody savannah, wetlands, evergreen needle forest, evergreen broadleaf forest, and urban, the mean daytime errors from the MODIS map are 1K or less and the standard deviations range between 2 and 4K. The nighttime differences have smaller biases, 0.5 to 1K, and reductions in the standard deviations compared to the daytime results. The largest values occur over heavily vegetated areas most likely because of cloud contamination and errors in the prescribed moisture loading. The ISCCP DX and VIRS results are similar to those for MODIS over heavily forested areas, but over other surface types, the magnitude of the predicted temperature errors are generally greater by 1 to 2K with much larger standard deviations. For MODIS during daytime, the largest errors arise urban and snow cases. The latter surface is most likely contaminated by clouds and rocks and forests for VIRS because of the latitudinal limitation of the sampling. Relatively pure snow surfaces are likely to occur relative to the polar regions. The urban cases are relatively poorly sampled. The Masuda model appears to produce small bias and rms errors over ocean. Surprisingly, the desert emissivities yield small biases and standard deviations during day and night. This result may be due to the general dryness and hence uncertainty of the atmospheric humidity over the deserts, lack of variable surface moisture, and minimal cloud contamination.

Table 3. T_3 errors using ϵ_3 and ϵ_4 for daytime and nighttime.

IGBP Type	$\Delta T(\text{K})$											
	From MODIS				From VIRS				From ISCCP DX			
	mean		std		mean		std		mean		std	
	Day	Night	Day	Night	Day	Night	Day	Night	Day	Night	Day	Night
1	1.4	-0.4	4.3	2.7	0.2	-0.7	4.1	2.7	0.3	-0.5	4.0	2.7
2	-1.8	-1.6	5.3	4.6	-3.2	-2.1	5.4	4.6	-3.0	-1.8	5.5	4.6
3	----	----	----	----	----	----	----	----	----	----	----	----
4	0.1	-0.4	4.4	3.3	-1.2	-0.9	4.4	3.2	-0.7	-0.7	4.4	3.2
5	0.6	-0.5	4.7	3.3	-0.4	-1.0	4.7	3.3	0.0	-0.7	4.6	3.3
6	-0.6	-0.2	5.5	3.2	-1.9	-0.8	5.3	3.1	-1.6	-0.5	5.4	3.2
7	0.3	-0.3	4.2	2.9	-1.4	-0.8	4.2	2.9	-0.7	-0.8	4.4	2.9
8	-1.1	-0.6	5.2	3.4	-2.1	-1.3	5.1	3.3	-1.9	-1.0	5.1	3.3
9	-0.7	-0.3	4.8	3.0	-1.9	-1.1	4.9	3.1	-1.7	-0.8	5.0	3.1
10	-0.8	-0.5	4.8	3.3	-1.8	-1.0	4.8	3.2	-1.5	-0.8	4.9	3.2
11	-1.0	-1.1	5.9	3.7	-1.3	-1.5	5.7	3.7	-0.9	-1.4	5.6	3.7
12	-0.5	-0.3	4.5	3.0	-1.6	-0.9	4.4	3.0	-1.3	-0.7	4.5	3.0
13	-2.6	-1.0	4.4	2.9	-3.7	-1.3	4.3	2.9	-3.8	-1.3	4.8	2.8
14	-0.5	-0.3	4.5	3.2	-1.6	-1.0	4.5	3.2	-1.3	-0.7	4.5	3.2
15	-1.8	-0.2	8.1	5.9	3.1	-1.0	7.5	5.8	-1.6	0.0	8.1	5.9
16	0.9	-0.5	3.6	2.6	-0.6	-0.8	3.4	2.4	0.0	-0.4	3.9	2.5
17	0.3	0.2	1.8	1.4	0.3	0.2	1.8	1.4	0.3	0.2	1.8	1.4
18	-2.1	-1.9	5.2	3.9	-2.9	-1.9	5.2	4.0	-4.4	-1.4	7.6	4.0
19	0.2	-0.6	5.4	3.1	0.5	-1.0	5.4	3.1	-0.3	-0.9	5.4	3.1

Table 4. T_3 errors using ϵ_3 and ϵ_4 for daytime and nighttime.

		$\Delta T(K)$											
IGBP Type	From MODIS				From VIRS				From ISCCP DX				
	mean		std		mean		std		mean		std		
	Day	Night	Day	Night	Day	Night	Day	Night	Day	Night	Day	Night	
1	-0.1	-0.2	3.0	2.1	-1.1	-1.2	2.9	2.0	0.0	-0.1	2.9	2.0	
2	-0.3	-0.1	2.7	2.1	-1.0	-0.6	2.7	2.0	-0.2	0.0	2.7	2.0	
3	----	----	----	----	----	----	----	----	----	----	----	----	
4	-0.5	-0.2	3.3	2.3	-1.5	-1.0	3.2	2.2	-0.5	-0.3	3.3	2.2	
5	-0.2	0.0	3.4	2.4	-1.2	-1.1	3.4	2.3	-0.2	-0.1	3.4	2.3	
6	-0.8	-0.2	3.6	2.0	-1.8	-1.0	3.5	2.0	-0.8	-0.1	3.5	1.9	
7	-0.6	-0.2	4.8	2.4	-1.9	-1.3	4.7	2.4	-0.5	0.0	4.7	2.4	
8	-0.4	-0.2	3.4	2.0	-1.3	-1.0	3.4	1.9	-0.3	-0.2	3.4	1.9	
9	-0.4	-0.3	3.2	1.9	-1.4	-1.1	3.1	1.8	-0.1	0.0	3.2	1.9	
10	-1.5	-0.5	5.6	2.7	-2.5	-1.3	5.6	2.7	-1.4	-0.3	5.6	2.7	
11	0.3	-0.4	2.8	2.1	-0.4	-1.1	3.1	2.5	0.3	-0.3	2.8	2.2	
12	-0.3	-0.1	3.2	2.1	-1.4	-1.0	3.1	2.0	-0.4	-0.1	3.1	2.0	
13	-1.9	-0.7	3.9	2.1	-2.8	-1.2	3.8	2.2	-2.1	-0.9	3.9	2.2	
14	-0.5	-0.2	3.3	1.9	-1.4	-0.9	3.2	1.9	-0.6	-0.3	3.2	1.9	
15	-1.2	0.6	8.0	5.9	-2.1	0.1	8.3	5.9	-0.9	0.8	7.9	5.9	
16	0.4	0.3	3.4	2.1	-1.1	-1.0	3.3	2.0	0.2	0.1	3.4	2.1	
17	0.3	0.2	1.2	1.1	0.3	0.2	1.2	1.1	0.3	0.2	1.2	1.1	
18	-3.3	-0.8	6.8	4.0	-4.0	-1.3	6.8	3.9	-2.7	-0.5	6.4	4.0	
19	-0.5	-0.6	3.9	2.2	-1.7	-1.7	3.8	2.3	0.1	0.0	3.9	2.1	

Overall, it appears that the MODIS-based channel-3 emissivities are better than either the VIRS or DX-based values. The temperature correction may account for some of the bias, but should not affect the standard deviations very much.

The error results for channel 5 are summarized in Table 4. In general, the biases and standard deviations are much lower than for channel 3. For the MODIS values, the errors are greatest for snow, tundra, and grassland. The VIRS-based emissivities produce much larger errors, possibly because of a day-night calibration difference [9]. The large errors for tundra, snow, and grassland suggest that cloud contamination was significant either in the observed data or in the derivation of the emissivities. The emissivities for 12- μm data are also more susceptible to errors in the humidity profile. Table 5 lists the errors that would be incurred if ϵ_3 were set equal to unity. The biases increase for the MODIS emissivities, while they appear to be much improved for the VIRS-based results. The biases for the DX emissivities switch signs and are slightly greater on average. Additional validation of the results is underway.

5. CONCLUDING REMARKS

This paper has presented the first empirical satellite-based global determination of surface emissivity for 3.7, 8.5, 10.8, and 12.0- μm . The results of the method applied here yield very reasonable daytime predictions of T_3 for the MODIS data that were used in the original determination of the emissivities. The resulting biases and variability in the day and night time data highlight the paucity of information about surface emissivity and the bidirectional reflectance characteristics at solar infrared (3.5 - 4.0 μm) wavelengths. The observed errors in the correction factors arise from spectral variability in surface emissivity, lack of aerosol corrections, uncertainties in the atmospheric profiles, VZA-dependencies, small time and space-scale changes of emissivity due to changes in surface moisture (e.g., dew), and residual cloud or ground fog contamination of the clear scenes. These and other factors will be explored to improve the determinations of surface emissivity for remote sensing. Additional MODIS data will be analyzed to determine the robustness of this technique and to determine the seasonal variability in surface emissivity.

Table 5. T_3 errors using ϵ_4 only for daytime and nighttime.

IGBP Type	$\Delta T(K)$											
	From MODIS				From VIRS				From ISCCP DX			
	mean		std		mean		std		mean		std	
	Day	Night	Day	Night	Day	Night	Day	Night	Day	Night	Day	Night
1	1.4	1.0	3.0	2.0	0.8	0.5	2.9	1.9	1.0	0.6	3.0	2.0
2	0.4	0.6	2.7	2.0	0.0	0.2	2.6	2.0	0.2	0.4	2.7	2.0
3	----	----	----	----	----	----	----	----	----	----	----	----
4	0.7	0.6	3.3	2.1	0.1	0.2	3.2	2.1	0.4	0.3	3.2	2.1
5	0.9	0.8	3.5	2.3	0.3	0.3	3.4	2.2	0.6	0.5	3.4	2.3
6	0.4	0.7	3.5	1.8	-0.2	0.2	3.4	1.8	0.0	0.4	3.4	1.8
7	1.3	1.4	4.8	2.3	0.3	0.4	4.7	2.2	0.7	0.9	4.7	2.3
8	0.8	0.9	3.4	1.9	0.2	0.4	3.4	1.8	0.5	0.6	3.4	1.8
9	1.1	1.1	3.2	1.8	0.3	0.3	3.1	1.8	0.6	0.6	3.1	1.8
10	0.1	0.8	5.6	2.6	-0.3	0.3	5.5	2.6	-0.1	0.6	5.5	2.6
11	1.2	0.5	2.6	2.0	1.0	0.2	2.7	2.0	1.1	0.3	2.7	2.0
12	1.0	1.1	3.2	2.0	0.3	0.4	3.1	1.9	0.5	0.7	3.1	1.9
13	-0.6	0.3	3.9	2.0	-1.1	0.0	3.9	2.0	-1.0	0.1	3.9	2.0
14	0.7	0.8	3.3	1.8	0.1	0.3	3.2	1.8	0.3	0.4	3.2	1.8
15	-0.6	1.0	7.9	5.9	-1.1	1.1	8.3	5.9	-0.2	1.4	7.9	6.0
16	2.8	2.2	3.4	2.1	1.6	1.1	3.3	1.9	2.4	1.7	3.4	2.1
17	0.7	0.6	1.2	1.0	0.7	0.6	1.2	1.0	0.7	0.6	1.2	1.0
18	-1.7	0.1	6.8	3.9	-1.9	-0.1	6.9	3.9	-1.2	0.3	6.5	3.9
19	0.9	0.6	3.8	2.0	0.5	0.3	3.8	2.0	0.6	0.4	3.8	2.0

REFERENCES

1. Wielicki, B. A., et al., Clouds and the Earth's Radiant Energy System (CERES): Algorithm overview. *IEEE Trans. Geosci. Remote Sens.*, **36**, 1127-1141, 1998.
2. Minnis, P., et al., Seasonal and diurnal variations of cloud properties derived for CERES from VIRS and MODIS data. *Proc. 11th AMS Conf. Atmos. Rad.*, Ogden, UT, June 3-7, 20-23, 2002.
3. Trepte, Q., Y. Chen, S. Sun-Mack, P. Minnis, D. F. Young, B. A. Baum, and P. W. Heck, Scene identification for the CERES cloud analysis subsystem. *Proc. AMS 10th Conf. Atmos. Rad.*, Madison, WI, June 28 – July 2, 1999, 169-172, 1999.
4. Minnis, P., W. L. Smith, Jr., and D. F. Young, Surface emissivity derived from multispectral satellite data. *Proc. 8th Annual ARM Sci. Team Mtg.*, Tuscon, AZ, March 23-27, 489-494, 1998.
5. Chen, Y., S. Sun-Mack, P. Minnis, W. L. Smith, Jr., and D. F. Young, Surface emissivity derived for infrared remote sensing from satellites. *Proc. AMS 11th Conf. Satellite Meteorology and Oceanography.*, Madison, WI, October 15-18, p4.36, 2001.
6. Kratz, D. P., The correlated k -distribution technique as applied to the AVHRR channels. *J. Quant. Spectrosc. Radiat. Transfer*, **53**, 501--517, 1995.
7. Rossow, W. B. and R. A. Schiffer, Advances in understanding clouds from ISCCP. *Bull Am. Meteor. Soc.*, **80**, 2261-2287, 1999.
8. Masuda, K., T. Takashima, and Y. Takayama, Emissivity of pure and sea waters for the model sea surface in the infrared window regions. *Remote Sens. Environ.*, **24**, 313-329, 1988.
9. Minnis, P., L. Nguyen, D. R. Doelling, D. F. Young, W. F. Miller, and D. P. Kratz, Rapid calibration of operational and research meteorological satellite imagers, Part II: Comparison of infrared channels. *J. Atmos. Oceanic Technol.*, **19**, 1250-1266, 2002.